

Bayesian deep learning for cosmic volumes with modified gravity

J.E. García-Farieta,^{1,2} Héctor J. Hortúa^{3,4} and Francisco-Shu Kitaura^{1,2}

¹ Instituto de Astrofísica de Canarias, s/n, E-38205, La Laguna, Tenerife, Spain e-mail: jorge.farieta@iac.es

² Departamento de Astrofísica, Universidad de La Laguna, E-38206, La Laguna, Tenerife, Spain

³ Grupo Signos, Departamento de Matemáticas, Universidad El Bosque, Bogotá, Colombia

⁴ Maestría en Ciencia de Datos, Universidad Escuela Colombiana de Ingeniería Julio Garavito, Bogotá, Colombia

Received September 15, 1996; accepted March 16, 1997

ABSTRACT

Context. The new generation of galaxy surveys will provide unprecedented data allowing us to test gravity deviations at cosmological scales at a much higher precision than achievable previously. A robust cosmological analysis of the large-scale structure demands exploiting the nonlinear information encoded in the cosmic web. Machine Learning techniques provide such tools, however, do not provide a priori assessment of uncertainties.

Aims. This study aims at extracting cosmological parameters from modified gravity (MG) simulations through deep neural networks endowed with uncertainty estimations.

Methods. We implement Bayesian neural networks (BNNs) with an enriched approximate posterior distribution considering two cases: one with a single Bayesian last layer (BLL), and another one with Bayesian layers at all levels (FullB). We train both BNNs with real-space density fields and power-spectra from a suite of 2000 dark matter only particle mesh N -body simulations including modified gravity models relying on MG-PICOLA covering $256 h^{-1}$ Mpc side cubical volumes with 128^3 particles.

Results. BNNs excel in accurately predicting parameters for Ω_m and σ_8 and their respective correlation with the MG parameter. Furthermore, we find out that BNNs yield well-calibrated uncertainty estimates overcoming the over- and under-estimation issues in traditional neural networks. We observe that the presence of MG parameter leads to a significant degeneracy with σ_8 being one of the possible explanations of the poor MG predictions. Ignoring MG, we obtain a deviation of the relative errors in Ω_m and σ_8 by at least 30%. Moreover, we report consistent results from the density field and power spectra analysis, and comparable results between BLL and FullB experiments which permits us to save computing time by a factor of two. This work contributes in setting the path to extract cosmological parameters from complete small cosmic volumes towards the highly nonlinear regime.

Key words. cosmology: – large-scale structure of Universe - cosmological parameters; methods: data analysis - statistical - numerical

1. Introduction

Cosmic acceleration is one of the most critical concerns in modern cosmology. In the context of the concordance model Λ CDM (Λ -Cold Dark Matter), this acceleration is attributed to the existence of a fluid with negative pressure that is represented by the cosmological constant, Λ , in general relativity (GR) equations. However, the existence of such fluid introduces some conceptual and theoretical issues that have not been fully addressed, either observational or theoretical. Alternative theories, such as modified gravity models, have attracted attention as a natural explanation for cosmic acceleration without invoking a cosmological constant (see, e.g., Nojiri et al. 2017, for a recent review). Among the plethora of alternative models, some parametrizations of $f(R)$ gravity have gained popularity due to their ability to reproduce the standard model’s predictions accurately. Indeed, both cosmological scenarios, Λ CDM and $f(R)$, are highly successful in providing an accurate description of the Universe on large scales, from cosmic microwave background (CMB) observations to the data of galaxy clustering (Berti et al. 2015).

Unlike the standard scenario, the $f(R)$ models do not require a cosmological constant but instead modify the behavior of

gravity itself. The modification of Einstein’s general relativity involves the addition of a scalar field that emulates cosmic acceleration. This feature of $f(R)$ models has made them perfect templates for tracking departures from standard gravity. Consequently, a crucial task within the scope of precision cosmology is to quantify the potential variations of gravity using appropriate techniques that are sensitive to modified gravity effects. Some of the approaches to achieve this aim include utilizing clustering anisotropies (Jennings et al. 2012; García-Farieta et al. 2019; Hernández-Aguayo et al. 2019; García-Farieta et al. 2020), tracer bias and sample selection (García-Farieta et al. 2021), cosmic voids (Voivodic et al. 2017; Perico et al. 2019; Contarini et al. 2021), halo mass functions (Hagstotz et al. 2019; Gupta et al. 2022) and peculiar velocities (Johnson et al. 2016; Ivarsen et al. 2016; Lyall et al. 2023).

Matter distribution is a rich source of cosmological information that has been exploited for many years through various techniques. One of the most used techniques to extract information from the large-scale structure (LSS) data, relies on the two-point statistics as described by the two-point correlation function or its equivalent in Fourier space, the matter power spectrum. Despite its success in capturing all possible cosmological information contained in a density field, it fails to capture features affected by the non-Gaussian nature of density perturbations, and its accuracy and precision cannot be relied

* jorge.farieta@iac.es

** hhortua@unbosque.edu.co

upon for probing small angular scales. Since the estimators up to second order do not contain all cosmological information, other techniques beyond the two-point statistics have been studied to extract the additional information such as N -point correlation functions (Peebles 2001; Takada & Jain 2003; Zhang et al. 2022; Brown et al. 2022; Veropalumbo et al. 2022; Philcox et al. 2022), Minkowski functionals (Kratochvil et al. 2012; Hikage et al. 2003; Fang et al. 2017), peak count statistics (Kacprzak et al. 2016; Peel et al. 2017; Fluri et al. 2018; Harnois-Déraps et al. 2021), density split statistics (Paillas et al. 2021), cosmic shear (Kilbinger 2015; Van Waerbeke et al. 2001), cosmic voids (Cai et al. (2015); Bos et al. (2012); Hamaus et al. (2016); Lavaux & Wandelt (2010)), and tomographic analysis based on the Alcock-Paczynski test (Park & Kim 2010; Zhang et al. 2019; Li et al. 2015; Luo et al. 2019; Dong et al. 2023). For a overview of contemporary cosmological probes, refer to Weinberg et al. (2013) and Moresco et al. (2022).

Recently, Deep Neural Networks (DNNs) have been proposed as a new alternative for not only recollecting the three-dimensional (3D) density field information without specifying beforehand the summary statistic such as the power spectrum but also, for managing the demanding computational needs in astrophysics (Dvorkin et al. 2022). The CNN algorithms have been explored as a valuable tool in modified gravity scenarios, mainly with applications in weak lensing maps as: emulator building (Tamosiunas et al. 2021) as well as to investigate observational degeneracies between modified gravity models and massive neutrinos (Merten et al. 2019; Peel et al. 2019), CMB patch maps analysis (Hortúa et al. 2020b), N-body simulations (Lazanu 2021; de Oliveira et al. 2020; Kodi Ramanah et al. 2020), but also Bayesian Neural Networks (BNNs) have been employed to identify and classify power spectra that deviate from Λ CDM such modified gravity models (Mancarella et al. 2022).

Despite their capability for extracting information from complex data, standard DNNs still suffer from overfitting/memorizing noisy labels during the training phase, and their point estimations are not always reliable. Bayesian Neural Networks (BNNs) are extensions from those DNNs that provide probabilistic properties on their outcomes and yield predictive uncertainties. These BNNs employ Variational Inference (VI) to infer posterior distributions for the weights suitable to capture uncertainties related to the network outputs (Graves 2011; Gunapati et al. 2022). Although VI speeds the computation of the posterior distribution when analytic approaches are considered, these assumptions can also introduce a bias (Charnock et al. 2022) that yields overconfident uncertainty predictions and significant deviations from the true posterior. In Hortúa et al. (2020a) and Hortúa (2021), the authors added normalizing flows on top of BNNs to give the joint parameter distribution more flexibility. However, that approach is not implemented into the Bayesian framework, still preserving the bias. In a recent work (Hortúa et al. 2023), the authors improved the previous methodology by applying multiplicative normalizing flows, resulting in accurate uncertainty estimates. In this paper, we follow the same approach by building BNNs models adapted to both 3D-density field and its power spectra to constrain modified gravity from cosmological simulations. We show that in the solely case of non-Gaussian signals it is possible to improve the posterior distributions and that when the additional information from the power spectrum is considered, they yield more significant performance improvements without underestimating the posterior distributions. This paper is organized as follows. Sec-

tion 2 offers a summary of structure formation in modified gravity cosmologies and the reference simulations created for training and testing the BNNs. In section 3 we briefly introduce the BNN concept and section 4 shows the architectures and configuration used in the paper. The results are presented in section 5 and an extended discussion of the findings is presented in section 6. Conclusions are given in section 7.

2. Large-scale structure in modified gravity

In this section, we present the gravity model which coincides with Λ CDM in the limiting case of a vanishing $f(R)$ parameter introduced below.

2.1. Structure formation and background

In $f(R)$ cosmologies, the dynamics of matter is determined by the modified Einstein field equations. The most straightforward modification of GR that circumvents Λ emerge by including a function of the curvature scalar in the Einstein-Hilbert action. In this modification, the equations of motion are enriched with a term that depends on the curvature scalar and that creates the same effect as dark energy (for a review on different MG models see e.g. Tsujikawa et al. 2008; De Felice & Tsujikawa 2010). For consistency across various cosmological scales, Hu & Sawicki (2007, hereafter HS) proposed a viable $f(R)$ function that is able to satisfy tight constraints at solar system scales, as well as accurately describe the dynamics of the Λ CDM background. In these models the modified Einstein-Hilbert action is given by

$$S_{\text{EH}} = \int d^4x \sqrt{-g} \left[\frac{R + f(R)}{16\pi G} \right], \quad (1)$$

where g is the metric tensor, G the Newton's gravitational constant, R the curvature scalar and $f(R)$ a scalar function that constrains the additional degree of freedom. In the HS model such function takes the form

$$f(R) = -m^2 \frac{c_1 (-R/m^2)^n}{c_2 (-R/m^2)^n + 1}, \quad (2)$$

where n, c_1, c_2 are model parameters, and $m^2 \equiv \Omega_m H_0^2$, with Ω_m being the present fractional matter density and H_0 the Hubble parameter at present time. For $n = 1$, which is the $f(R)$ model we will consider in this paper the function can be written as follows

$$f(R) \approx -2\Lambda + |f_{R0}| \frac{R_0^2}{R}. \quad (3)$$

Here f_{R0} represents the dimensionless scalar field at present time, meaning the only additional degree of freedom that stems from the derivative of $f(R)$ with respect to the curvature scalar, f_R . The modified Einstein field equations and analogous Friedmann equations that describe the HS model's background can be obtained from minimizing the action (for a thorough derivation see Song et al. 2007). To further understand the formation and evolution of large-scale structures in MG, it is crucial to describe the matter perturbations, δ_m , around the background (see Song et al. 2007). The MG effects are captured by the growth of density perturbations in the matter dominated era when mildly nonlinear regime is important (Laszlo & Bean 2008). In particular, when considering linear perturbations, the equations of the evolution of matter overdensities in Fourier space are as follows

(Tsujikawa 2008):

$$\begin{aligned} \ddot{\delta}_m + \left(2H + \frac{\dot{F}}{2F}\right) \dot{\delta}_m - \frac{\rho_m}{2F} \delta_m \\ = \frac{1}{2F} \left[\left(-6H^2 + \frac{k^2}{a^2} \right) \delta F + 3H\delta\dot{F} + 3\delta\ddot{F} \right], \\ \delta\ddot{F} + 3H\delta\dot{F} + \left(\frac{k^2}{a^2} + \frac{F}{3F_R} - 4H^2 - 2\dot{H} \right) \delta F = \frac{1}{3} \delta\rho_m + \dot{F}\dot{\delta}_m, \end{aligned} \quad (4)$$

with H being the Hubble parameter, k the comoving wavenumber of the perturbations, a the scale factor, ρ_m the matter density field and $F \equiv \partial f/\partial R$. The solution to system of Eqs. (4) provides a detail description of δ_m , which includes most of the cosmological information, since it is a direct result of the gravitational interaction of cosmic structures. In fact, to get insights into the underlying cosmic parameters, the density field is the primary source to be investigated using summary statistics. The Eqs. (4) make evident the connection between the density field and the scalaron of MG. Consequently, any departure from the GR would be measurable through the density field, either with the structure growth rate or its tracer distribution. A particular feature of the $f(R)$ models is the so-called *chameleon mechanism*. This mechanism reconciles the departures of GR with the bounds imposed by local tests of gravity. It endows the mass of the scalar field with the ability to depend on the local matter density. More precisely, the signatures of MG can be detected in regions of lower matter density where the scalar field becomes lighter, leading to potential observable effects that deviate from standard gravity.

The 3D matter power spectrum, denoted as $P(k)$, is the primary statistical tool employed to extract cosmological insights from the density field. It characterizes the overdensities as a function of scale and is estimated through the following average over Fourier space:

$$(2\pi)^3 P(\mathbf{k}) \delta_D^3(\mathbf{k} - \mathbf{k}') = \langle \delta(\mathbf{k}) \delta(\mathbf{k}') \rangle, \quad (5)$$

where δ_D^3 is the three-dimensional Dirac-delta function. This function contains all information from the statistics of the density field in the linear regime, and a decreasing fraction of the total information on smaller scales, if initial density fields followed Gaussian statistics. In this work we use the Pylians3¹ library to estimate the overdensity field as well as the power spectrum.

2.2. Modified gravity simulations

The simulations were created with the COmoving Lagrangian Acceleration (COLA) algorithm (Tassev et al. 2013; Koda et al. 2016), which is based on a Particle-Mesh code that solves the equations of motion following the Lagrangian Perturbation Theory (LPT) trajectories of the particles. This algorithm speed up the computation of the gravitational force using a very few timesteps and still get correct results on the largest scales. In particular we used MG-PICOLA² (Winther et al. 2017), a modified version of L-PICOLA (Howlett et al. 2015) that has been extensively tested against full N-body simulations and that extends the gravity solvers to MG models, including the HS parametrization.

We run a set of 2500 MG simulations varying four cosmological

Table 1. The summary of the set-up of the MG simulations. Left: cosmology parameters. Right: set-up parameters used for MG-PICOLA code.

Cosmologies		Simulation setup	
Ω_m	[0.1, 0.5]	Boxsize	$256 h^{-1}$ Mpc
h	[0.5, 0.9]	N_p	128^3
σ_8	[0.6, 1.0]	Grid force	128^3
$0.1 \log_{10} f_{R0} $	[0.4, 0.6]	IC	2LPT $z_{ini} = 49$
Ω_b	0.0489	Steps	100
n_s	0.9665	k_{Ny}	1.58

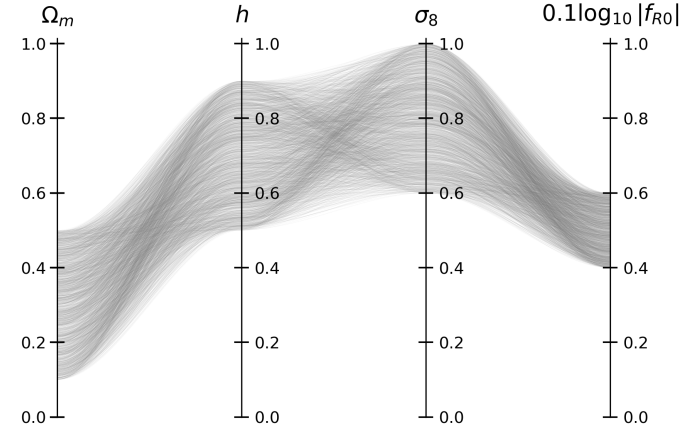


Fig. 1. Diagram illustrating the multidimensional parameter space variations. Each line represents a data point's parameter values, with four parameters $\{\Omega_m, h, \sigma_8, 0.1 \log_{10} |f_{R0}|\}$ visualized along separate axes.

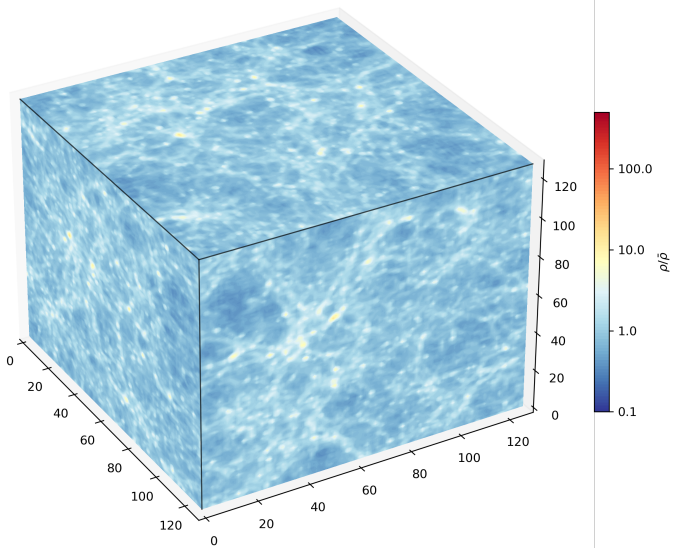


Fig. 2. The projected overdensity field at redshift $z = 0$ derived from an arbitrary chosen simulation within the ensemble of 2500 MG simulations. The normalized density field was calculated using a CIC mass assignment scheme.

parameters $\Theta = \{\Omega_m, h, \sigma_8, f_{R0}\}$, where h is the reduced Hubble parameter, σ_8 the r.m.s. density fluctuation within a top-hat sphere of $8 h^{-1}$ Mpc radius and f_{R0} the amplitude of the modified gravity function in the HS model. The remaining cosmological parameters are set to $\Omega_b = 0.048206$ and $n_s = 0.96$, which correspond to the values reported by Planck Collaboration et al.

¹ <https://pylians3.readthedocs.io/en/master/index.html>

² The code can be found at <https://github.com/HAWinther/MG-PICOLA-PUBLIC>

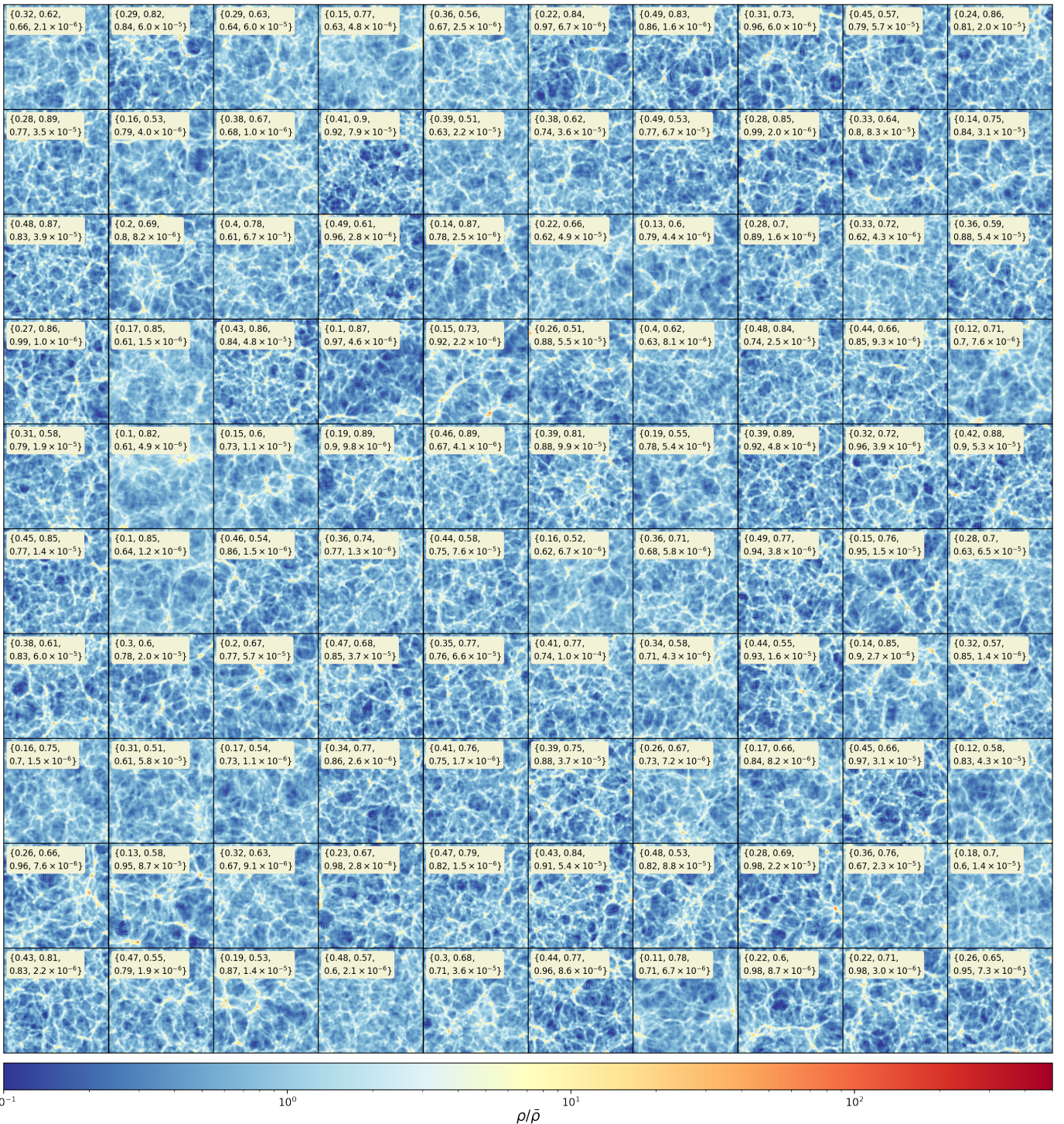


Fig. 3. Projected density field of dark matter in a region of $256 \times 256 \times 20 (h^{-1} Mpc)^3$ from 100 out of 2500 simulations of MG arbitrarily chosen. The snapshots are taken at $z = 0$ and the legend displays the set of cosmological parameters to be $\{\Omega_m, h, \sigma_8, f_{R0}\}$. The cuts in the density field highlight the broad coverage of the parameter space of the MG simulations. Different features can be observed by naked-eye, such as variations in the filamentary structure of the cosmic web.

(2020). The parameter space is sampled with random numbers uniformly distributed within the specified ranges for each parameter (see Table 1). Since the typical values of the modified gravity parameter goes as powers of ten, $|f_{R0}| \sim 10^n$ with $n \in [-4, -6]$, we choose to sample a fraction of its logarithm in order to cover the range of powers equally, i.e., $\tilde{f}_{R0} = 0.1 \log_{10} |f_{R0}|$. Figure 1

illustrates the parameter space variations of the 2500 MG cosmologies, each one is represented by a gray line. The values of the cosmological parameters, Θ , are distributed along the different vertical axis. Each simulation follows the dynamics of 128^3 particles in a small box of comoving side-length $256 h^{-1} \text{Mpc}$ using 100 timesteps from an initial redshift $z_i = 49$ up to redshift $z = 0$. This simulation resolution allows us to reasonably

investigate the impacts of MG on large scales, in particular for the f_{R0} values considered in this work. However, it is not as effective at very small scales, where higher resolution is required. In fact, MG solvers have undergone extensive testing using low-resolution simulations (see, for example, Puchwein et al. (2013); Li et al. (2012); Hernández-Aguayo et al. (2022)). These tests show the enhancement of the power spectrum in simulations of $256 h^{-1} \text{ Mpc}$, where MG effects begins to be appreciable. The setup of the MG simulations used in this work is summarized in Table 1. In a recent research, a similar setup was employed with light-weight deterministic CNN to estimate a subset of parameters of a flat ΛCDM cosmology (Pan et al. 2020), however in this work we choose a time-step larger by a factor of 2.5. The initial conditions for the MG simulations were created with 2LPTic (Crocce et al. 2006, 2012) based on a ΛCDM template at z_i , moreover, a distinct random seed was assigned to each simulation to generate varying distributions of large-scale power. This approach allows our neural network to effectively capture the inherent cosmic variance.

We calculate the overdensity field, δ_m , for each snapshot at redshift $z = 0$, employing the cloud-in-cell (CIC) mass assignment scheme (Hockney & Eastwood 1981) on a regular grid consisting of $N^3 = 128^3$ voxels. The training set comprises 80% of the data, which corresponds to 2000 boxes containing the overdensity fields, while the remaining 20% of the data was used for testing. Fig. 2 displays the 3D overdensity field plus the unity, $\delta_m + 1 = \rho_m/\bar{\rho}_m$, projected along each plane of the box. The displayed data corresponds to an arbitrarily chosen combination of parameters within the MG simulation suite at redshift $z = 0$. Similarly, Fig. 3 displays the 2D density field of dark matter in a region of $256 \times 256 \times 20 (h^{-1} \text{ Mpc})^3$ from 100 out of 2500 simulations of MG arbitrarily chosen, with the cosmological parameter combination as indicated by the labels. The cuts in the density field provides a visual means to discern distinct features of the cosmic web, observable to the naked eye. These features include variations in the filamentary structure of the cosmic web, which become evident in the zones of under- and over-densities. Additionally, we output the matter power spectrum of all realizations by directly computing the modulus of each Fourier mode from the particle distribution, $|\delta_m(k)|^2$. The Fig. 4 shows the different matter power spectrum for the entire MG simulation suit. The variations in the shape of the spectrum correspond to the joint effect of cosmological parameters that were varied as shown in the label. We consider the effective range of the power spectrum up to the Nyquist frequency, k_{Ny} , which in our simulations corresponds to $k \approx 1.58 \text{ Mpc}/h$. The full datasets used in this paper, 3D overdensity fields as well as power spectra, are publicly available in Zenodo³.

3. Bayesian Neural Networks

The primary goal of Bayesian Neural Networks (BNNs) is to estimate the posterior distribution $p(w|\mathcal{D})$, which represents the probability distribution of the weights w of the network given the observed data $\mathcal{D} = (X, Y)$ (Abdar et al. 2021; Gal 2016; Graves 2011). The posterior distribution, denoted as $p(w|\mathcal{D})$, can be derived using Bayes' law: $p(w|\mathcal{D}) \sim p(\mathcal{D}|w)p(w)$. This expression involves a likelihood function, $p(\mathcal{D}|w)$, which represents the probability of the observed data \mathcal{D} given the weights w , as well as a prior distribution on the weights, denoted as $p(w)$. After the computation of the posterior, the probability distribution of a

³ Data will be available upon publication. Please contact the authors for earlier access

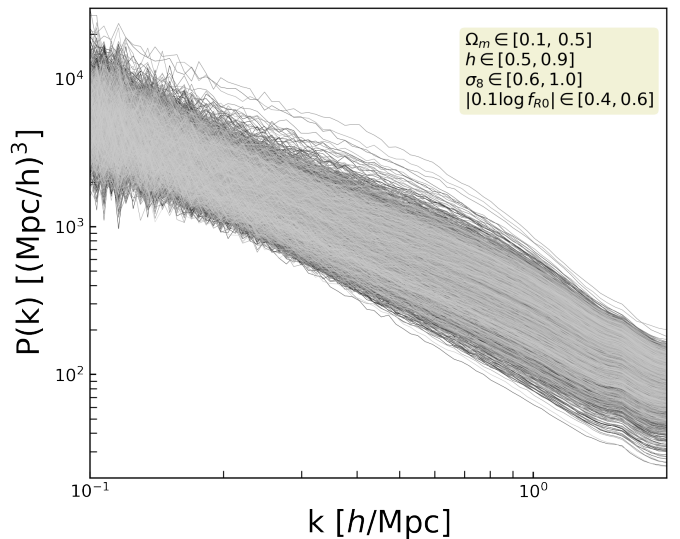


Fig. 4. The matter power spectrum at $z = 0$ of the MG simulation suit. The variations in the spectrum correspond to changes in each of the four parameters that were varied, $\{\Omega_m, h, \sigma_8, |0.1 \log f_{R0}|\}$. The corresponding range of each of parameter is shown in the label.

new test example x^* can be determined by

$$p(y^*|x^*, \mathcal{D}) = \int_w p(y^*|x^*, w)p(w|\mathcal{D})dw, \quad (6)$$

being $p(y^*|x^*, w)$ the predictive distribution corresponding to the set of weights. In the context of neural networks, it is important to note that the direct computation of the posterior is not feasible (Gal 2016). To circumvent this limitation, variational inference (VI) techniques approximating the posterior distribution have been introduced (Graves 2011). VI considers a family of simple distributions, denoted as $q(w|\theta)$, which is characterized by a parameter θ . The objective of VI is to identify a distribution $q(w|\theta^*)$ that minimizes the Kullback-Leibler divergence between $q(w|\theta)$ and $p(w|\mathcal{D})$, where θ^* represents the optimal parameter values, being $KL[\cdot||\cdot]$ the Kullback-Leibler (KL) divergence. This minimization is equivalent to maximizing the evidence lower bound (ELBO) (Gal 2016),

$$\text{ELBO}(\theta) = \mathbb{E}_{q(w|\theta)}[\log p(Y|X, w)] - KL[q(w|\theta)||p(w)], \quad (7)$$

where $\mathbb{E}_{q(w|\theta)}[\log p(Y|X, w)]$ is the expected log-likelihood with respect to the variational posterior and $KL[q(w|\theta)||p(w)]$ is the divergence of the variational posterior from the prior. It can be observed from Eq. (7) that the Kullback-Leibler (KL) divergence serves as a regularizer, compelling the variational posterior to shift towards the modes of the prior. A frequently employed option for the variational posterior entails utilizing a product of independent Gaussian distributions, specifically mean-field Gaussian distributions, with each parameter w being associated with its own distribution (Abdar et al. 2021)

$$q(w|\theta) = \prod_{ij} \mathcal{N}(w; \mu_{ij}, \sigma_{ij}^2), \quad (8)$$

where i and j are the indices of the neurons from the previous-and the current layers, respectively. Applying the reparametrization trick we obtain $w_{ij} = \mu_{ij} + \sigma_{ij} * \epsilon_{ij}$, where ϵ_{ij} is drawn from the normal distribution. Moreover, if the prior is a composition of independent Gaussian distributions, the KL-divergence between

the prior and the variational posterior can be calculated analytically. This characteristic enhances the computing efficiency of this approach.

3.1. Multiplicative normalizing flows

Gaussian mean-field distributions described in Eq. (8) are the most commonly utilized family for the variational posterior in BNNs. Unfortunately, this distribution lacks the capacity to adequately represent the intricate nature of the true posterior. Hence, it is anticipated that enhancing the complexity of the variational posterior will yield substantial improvements in performance. This is attributed to the capability of sampling from a more reliable distribution, which closely approximates the true posterior distribution. Indeed, the process of improving the variational posterior demands efficient computational methods while ensuring its numerical feasibility. Multiplicative Normalizing Flows (MNFs) have been proposed to efficiently adapt the posterior distributions through the utilization of auxiliary random variables and the normalizing flows (Louizos & Welling 2017). Mixture normalizing flows (MNFs) suggest that the variational posterior can be mathematically represented as an infinite mixture of distributions

$$q(w|\theta) = \int q(w|z, \theta)q(z|\theta)dz, \quad (9)$$

with θ the learnable posterior parameter, and $z \sim q(z|\theta) \equiv q(z)$ ⁴ the vector with the same dimension of the input layer, which plays the role of an auxiliary latent variable. Also, allowing for local reparametrizations, the variational posterior for fully connected layers becomes

$$w \sim q(w|z) = \prod_{ij} \mathcal{N}(w; z_i \mu_{ij}, \sigma_{ij}^2). \quad (10)$$

Where we can increase the flexibility of the variational posterior by enhancing the complexity of $q(z)$. This can be done using normalizing flows since the dimensionality of z is much lower compared to the weights. Starting from samples $z_0 \sim q(z_0)$ from fully factorized Gaussians (see Eq. (8)), a rich distribution $q(z_K)$ can be obtained by applying successively invertible f_k -transformations

$$z_K = \text{NF}(z_0) = f_K \circ \dots \circ f_1(z_0), \quad (11)$$

$$\log q(z_K) = \log q(z_0) - \sum_{k=1}^K \log \left| \det \frac{\partial f_k}{\partial z_{k-1}} \right|. \quad (12)$$

To handle the intractability of the posterior, Louizos & Welling (2017) suggest to use again Bayes law $q(z_K)q(w|z_K) = q(w)q(z_K|w)$ and introduce a new auxiliary distribution $r(z_K|w, \phi)$ parameterized by ϕ , with the purpose of approximating the posterior distribution of the original variational parameters $q(z_K|w)$ to further lower the bound of the KL divergence term. Accordingly, the KL-divergence term can be rewritten as follows

$$-\text{KL}[q(w)\|p(w)] \geq \mathbb{E}_{q(w,z_K)} \left[-\text{KL}[q(w|z_K)\|p(w)] + \log q(z_K) + \log r(z_K|w, \phi) \right]. \quad (13)$$

⁴ For the sake of clarity in notation, the parameter θ will no longer be considered in the subsequent discussion.

The first term can be analytically computed since it will be the KL-divergence between two Gaussian distributions, while the second term is computed via the normalizing flow generated by f_K (see Eq. (12)). Furthermore, the auxiliary posterior term is parameterized by inverse normalizing flows as follows (Touati et al. 2018)

$$z_0 = \text{NF}^{-1}(z_K) = g_1^{-1} \circ \dots \circ g_K^{-1}(z_K), \quad (14)$$

and

$$\log r(z_K|w, \phi) = \log r(z_0|w, \phi) + \sum_{k=1}^K \log \left| \det \frac{\partial g_k^{-1}}{\partial z_k} \right|, \quad (15)$$

where one can parameterize g_K^{-1} as another normalizing flow. A flexible parametrization of the auxiliary posterior can be given by

$$z_0 \sim r(z_K|w, \phi) = \prod_i \mathcal{N}(z_0; \tilde{\mu}_i(w, \phi), \tilde{\sigma}_i^2(w, \phi)), \quad (16)$$

where the parameterization of the mean $\tilde{\mu}$, and the variance $\tilde{\sigma}^2$ is carried out by the masked RealNVP (Dinh et al. 2017) as the choice of normalizing flows.

3.2. Multiplicative normalizing flows in voxel-grid representation

In this section we present our first result, where we have generalized Eq. (10) to 3D convolutional layers where cosmological simulated data are structured. To this end, we started with the extension of sampling from the variational posterior as

$$w \sim q(w|z) = \prod_i^{D_d} \prod_j^{D_h} \prod_k^{D_w} \prod_l^{D_f} \mathcal{N}(w; z_l \mu_{ijkl}, \sigma_{ijkl}^2), \quad (17)$$

where D_h , D_w , D_d are three spatial dimensions of the boxes,

Algorithm 1 Forward propagation for each Convolutional 3D layer. M_w , Σ_w are the means and variances of each layer, H is the input layer, and $\text{NF}(\cdot)$ is the masked RealNVP normalizing flow. \odot corresponds to element-wise multiplication.

```

 $H \leftarrow$  Input conv3D-layer (minibatch)
 $z_0 \sim q(z_0)$ 
 $z_{T_f} = \text{NF}(z_0)$ 
 $M_h = H * (M_w \odot \text{reshape}(z_{T_f}, [1, 1, 1, D_f]))$ 
 $V_h = H^2 * \Sigma_w$ 
 $E \sim \mathcal{N}(0, 1)$ 
return  $M_h + \sqrt{V_h} \odot E$ 

```

and D_f is the number of filters for each kernel. The objective is to address the challenge of enhancing the adaptability of the approximate posterior distribution for the weight coming from a 3D-convolutional layer. Algorithm 1 outlines the procedure to forward propagation for each 3D-convolutional layer. Similar to the fully connected case, the auxiliary parameter affects only the mean with the purpose of avoiding large variance and we kept a linear mapping to parametrize the inverse normalizing flows instead of applying tanh feature transformations.

Table 2. Configuration of the (Se)-ResNet backbone used for all experiments presented in this paper.

(Se)-ResNet-18 backbone		
Layer Name	Input Shape	Output Shape
Batch Norm	(N_{batch} , 128,128,128,1)	(N_{batch} , 128,28,128,1)
3D Convolutional	(N_{batch} , 128,128,128,1)	(N_{batch} , 64,64,64,16)
Batch Norm+ReLU	(N_{batch} , 64,64,64,16)	(N_{batch} , 64,64,64,16)
Max Pooling 3D	(N_{batch} , 64,64,64,16)	(N_{batch} , 32,32,32,16)
Batch Norm+ReLU	(N_{batch} , 32,32,32,16)	(N_{batch} , 32,32,32,16)
Resblock 1	$\begin{bmatrix} (N_{\text{batch}}, 32, 32, 32, 16) \\ (N_{\text{batch}}, 16, 16, 16, 32) \end{bmatrix}$	(N_{batch} , 16,16,16,32)
Batch Norm+ReLU	(N_{batch} , 16,16,16,32)	(N_{batch} , 16,16,16,32)
Resblock 2	$\begin{bmatrix} (N_{\text{batch}}, 16, 16, 16, 32) \\ (N_{\text{batch}}, 8, 8, 8, 64) \end{bmatrix}$	(N_{batch} , 8,8,8,64)
Batch Norm+ReLU	(N_{batch} , 8,8,8,64)	(N_{batch} , 8,8,8,64)
Resblock 3	$\begin{bmatrix} (N_{\text{batch}}, 8, 8, 8, 64) \\ (N_{\text{batch}}, 4, 4, 4, 128) \end{bmatrix}$	(N_{batch} , 4,4,4,128)
Batch Norm+ReLU	(N_{batch} , 4,4,4,128)	(N_{batch} , 4,4,4,128)
Resblock 4	$\begin{bmatrix} (N_{\text{batch}}, 4, 4, 4, 128) \\ (N_{\text{batch}}, 2, 2, 2, 256) \end{bmatrix}$	(N_{batch} , 2,2,2,256)
Batch Norm+ReLU	(N_{batch} , 2,2,2,256)	(N_{batch} , 2,2,2,256)
Global Avg Pooling	(N_{batch} , 2,2,2,256)	(N_{batch} , 256)

4. The Bayesian architecture set-up

We will examine four distinct architectures of Bayesian Neural Networks (BNNs) as outlined in Section 3. Two of these architectures include Bayesian layers located only on the top of the network, the so-called Bayesian Last Layer (denoted as **BLL**), while the remaining have Bayesian layers at all their levels (**FullB**). The pipelines utilized in our study were developed using [TensorFlow v:2.12](#) and [TensorFlow-probability v:0.19](#) (Abadi et al. 2015). The architecture used for all networks has ResNet-18 as the backbone, which is depicted in a schematic manner in Table 2. The Resblock nature depends on whether we build either ResNet or SeResNet topology. The latter is a variant of ResNet that employs squeeze-and-excitation blocks that adaptively recalibrate channel-wise feature responses by explicitly modeling interdependencies between channels (Hu et al. 2019). Fig. 5 depicts each Resblock and how the skip connections are defined. These architectures were designed using the GIT repository [classification-models-3D](#). ResNet18 contains 2510149 trainable parameters while SeResNet has 3069270 but, these numbers are duplicates when we move towards a fully Bayesian scheme because two parameters need to be optimized (the mean and standard deviation) for each network parameter. In this study, 50 layers were employed for the masked RealNVP normalizing flow. The development of these convolutional layers was made using also the repositories [TF-MNF-VBNN](#) and [MNF-VBNN](#) (Louizos & Welling 2017). Finally, all networks end with a multivariate Gaussian distribution layer, consisting of fourteen trainable parameters. These parameters include four means, denoted as μ , which correspond to the cosmological parameters, as well as ten elements representing the covariance matrix Σ . The loss function to be optimized is given by the ELBO, Eq. (7), where the second term is associated with the negative

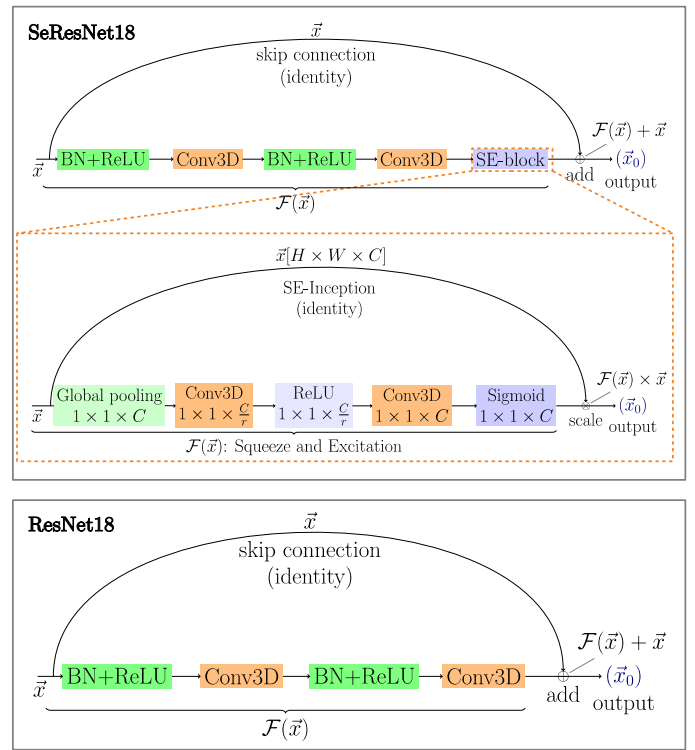


Fig. 5. Resblock schema depending on the architecture used. Top: Resblock when SeResNet18 is employed. The orange dashed rectangle shows the skip SE-connection schema used in the SeResNet18 resblock. Bottom: Resblock when ResNet is employed.

log-likelihood (NLL)

$$-\text{NLL} \sim \frac{1}{2} \log |\Sigma| + \frac{1}{2} (\mathbf{y} - \boldsymbol{\mu})^\top (\Sigma)^{-1} (\mathbf{y} - \boldsymbol{\mu}), \quad (18)$$

averaged over the mini-batch. The optimizer used was Adam with first and second moments exponential decay rates of 0.9 and 0.999, respectively (Kingma & Ba 2014). The learning rate starts from 5×10^{-4} and it is reduced by a factor of 0.9 in case any improvement has not been observed after 8 epochs. Furthermore, we have applied a warm-up period for which the model turns on progressively the KL term in Eq. (7). This is achieved by introducing a β variable in the ELBO, i.e., $\beta \cdot \text{KL}[q(w|\theta) \| p(w)]$, so, this parameter starts being equal to 0 and grows linearly to 1 during 12 epochs (Sønderby et al. 2016). BNNs were trained with 8 batches and early stopping callback was presented to avoid overfitting. The infrastructure put in place by Google Cloud Platform (GCP) uses a nvidia-tesla-t4 of 16 GB GDDR6 in a N1 machine series shared-core.

4.1. Quantifying the performance

The metrics employed for determining the network performance were the Mean Square Error (MSE), ELBO, and the coefficient of determination r^2 . Moreover, we quantify the quality of the uncertainty estimates through reliability metrics. Following Laves et al. (2020) and Guo et al. (2017), we can define a perfect calibration of regression uncertainty as

$$\mathbb{E}_{\hat{\sigma}^2} [\text{abs}[(\|\mathbf{y} - \boldsymbol{\mu}\|^2 | \hat{\sigma}^2 = \alpha^2) - \alpha^2]] \quad \forall \{\alpha^2 \in \mathbb{R} | \alpha^2 \geq 0\}, \quad (19)$$

being $\text{abs}[\cdot]$ the absolute value function. So, the predicted uncertainty $\hat{\sigma}^2$ is partitioned into K bins with equal width, to variance

per bin is defined as

$$\text{var}(B_k) := \frac{1}{|B_k|} \sum_{i \in B_k} \frac{1}{N} \sum_{n=1}^N (\mu_{i,n} - y_i)^2, \quad (20)$$

with N stochastic forward passes. In addition, the uncertainty per bin is defined as

$$\text{uncert}(B_k) := \frac{1}{|B_k|} \sum_{i \in B_k} \hat{\sigma}_i^2, \quad (21)$$

allow us to compute the expected uncertainty calibration error (UCE) in order to quantify the miscalibration

$$\text{UCE} := \sum_{k=1}^K \frac{|B_k|}{m} |\text{var}(B_k) - \text{uncert}(B_k)|, \quad (22)$$

with the number of inputs m and set of indices B_k of inputs, for which the uncertainty falls into the bin k .

5. Results

In this section, we present the results of several experiments developed to quantify the performance of Bayesian deep learning neural networks for constraining the cosmological parameters in modified gravity scenarios.

5.1. Parameter estimation from the overdensity field under voxel-grid representation

Using the configuration described in Sec. 4, we designed four experiments inspired by two successful deep learning architectures, ResNet18 and Se-ResNet18. The former is a residual network commonly known due to its efficiency in several computer vision tasks, while the latter has been chosen because of its ability to improve the interdependencies between the channels of convolutional feature layers (Hu et al. 2019). Furthermore, the modification of the models was also based on the insertion of a set of Bayesian layers at either the top of the model (BLL), or in the entire architecture (FullIB). The motivation for exploring both possibilities comes from the fact that intuitively, adding a Bayesian layer at the end of the network (BLL), can be viewed as Bayesian linear regression with a learnable projected feature space, allowing for a successful balance between scalability and the degree of model-agnosticism (Fiedler & Lucia 2023; Watson et al. 2021). On the contrary, although fully Bayesian networks (FullIB) would demand high computational resources, it has been reported that their Bayesian hidden layers are susceptible to out-of-distribution (OOD) examples that might improve predictive uncertainty estimates (Henning et al. 2021). The results of the experiments performed in this work are summarized in Table 3. Here we can observe the performance of each architecture on the test set. In the top part of the table, the results of SeResNet18 topology are shown, while in the bottom part, the results of ResNet18 are presented. The left columns of the table correspond to the FullIB scheme, while the left one to the Bayesian Last Layer, BLL. Comparing all approaches, we observe that FullIB-SeResNet18 slightly outperforms the rest of the models in terms of accuracy (described by r^2) and uncertainty quality provided by UCE. However, significant differences were not found in the reported metrics for ResNet and its SeResNet counterpart, except for the inference time where the BLL models clearly outperform the FullIB ones. This brings the idea that FullIBs yield

small improvements in the computation of uncertainties at the expense of duplicating the inference time. In addition, both architectures estimate σ_8 more efficiently than for any other parameter, especially in contrast to h or $0.1 \log_{10} |f_{R0}|$, although the FullIBs respond slightly better to MG effects. Fig. 6 displays the scatter relationship between the predicted and ground truth values of each cosmological parameter using FullIB-SeResNet18. It also shows the degeneracy directions that arise from observations defined as $\Omega_m h^2$ and $\sigma_8 \Omega_m^{0.25}$. The diagonal gray lines correspond to the ideal case of a perfect parameter prediction. Each data point represents the mean value of the predicted distributions, and the error bars stand for the heteroscedastic uncertainty associated with epistemic plus aleatoric uncertainty at $1-\sigma$ confidence level. As we observe, BNNs learn how to accurately predict the value for Ω_m and σ_8 , but they fail in capturing information related to the MG effects and the Hubble parameter. Even though parameter estimation derives from all features of the fully nonlinear 3D overdensity field, the horizontal scatter pattern that exhibits the Hubble and MG parameters implies that essential underlying connections are not effectively captured. A similar result for the Hubble parameter using DCNNs in Λ CDM can be found in Villaescusa-Navarro et al. (2020).

5.2. Parameter estimation coming from the matter power spectrum

In this section, we show the results of using the power spectrum to extract the cosmological parameters in MG scenarios.

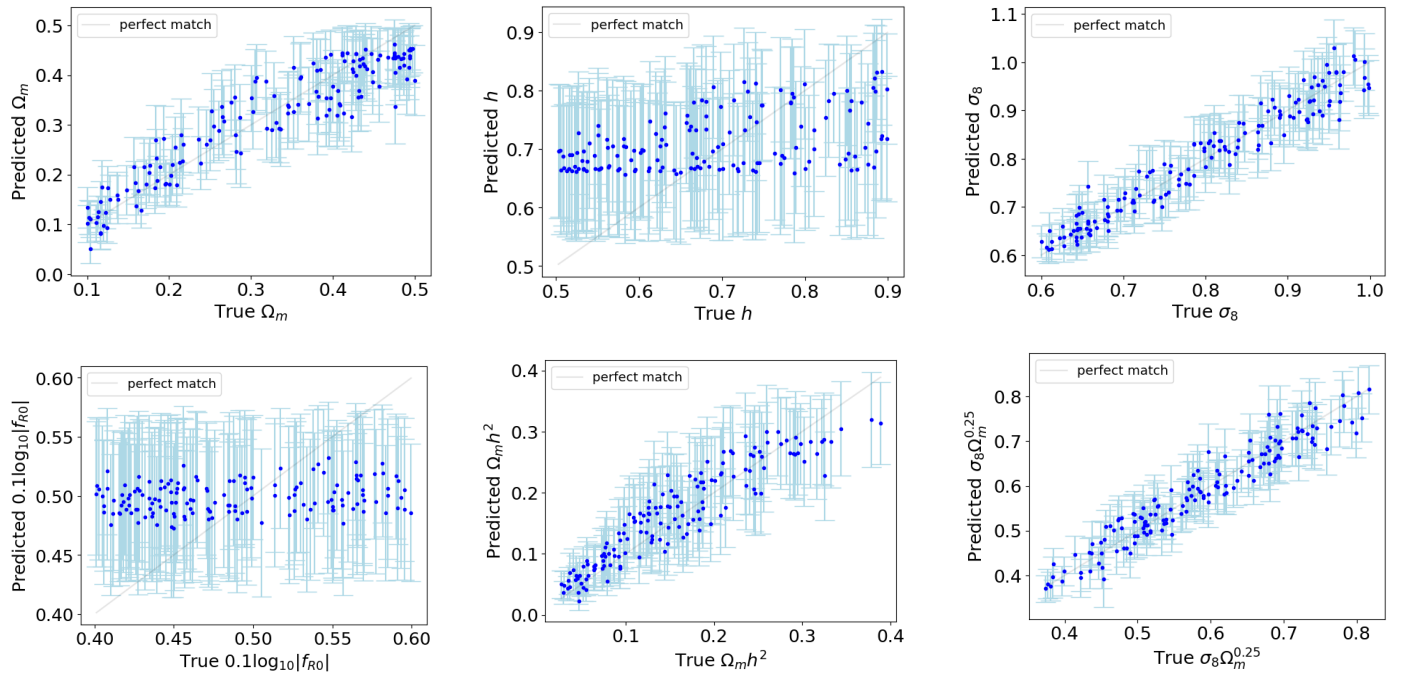
Following the same methodology as described in the voxel-grid representation, we implement two BNN models that provide distributed predictions for the cosmological parameters. Table 4 schematically presents the architecture used for this purpose. This represents a Fully Connected Network (FCN) with 60000 trainable parameters, and it was derived from KerasTuner⁵ as a framework to make scalable hyperparameter optimization. We work with a Bayesian Last Layer model (BLL-FCN) along with a Full Bayesian topology where all dense layers are probabilistic (FullIB-FCN). Here, the power spectrum computed from the N-body simulations is kept until $k \approx 1.58 h^{-1}$ Mpc, obtaining arrays of 85 dimensions. The results of this approach are shown in Table 5. In contrast to the voxel-grid representation where the Full Bayesian approach outperforms most of the models, here we clearly observe that BLL approach works better than the fully Bayesian one. These results show a similar performance compared to the 3D overdensity field. We expected this behavior since most of the voxel-grid information should be encoded into the two-point correlator. Notice also that some parameters such as σ_8 or the derived parameters provide higher accuracy when they are predicted with the voxel-grid approach supporting the fact that 3D-convolutional layer extracts further information beyond the linear part. The interplay between the f_{R0} parameter and the shape of the power spectrum is essential for testing and constraining gravity theories. The immediate effect of f_{R0} on the power spectrum is to modulate its amplitude, most notably at small scales. Furthermore, this parameter of the HS model exhibits a substantial degeneracy with σ_8 , which produces a similar effect on the power amplitude, but not in a scale-dependent manner as MG does. The strongest deviations of the power spectrum from the Λ CDM model are observed for high values of f_{R0} , in our case $\sim 10^{-4}$ (see Fig. 4). Because of this degeneracy, it is probable that some of the MG information is being encoded in the σ_8 parameter rather than the f_{R0} parameter. This hypothesis,

⁵ https://keras.io/keras_tuner/

Table 3. Metrics for the test set for all BNNs architectures. Top: SeResNet18, bottom: ResNet18. High UCE values indicate miscalibration. Bold text is the minimum (maximum) value, ↓ (↑) as indicated in the metric name, among the different parameters.

Metrics	FullB-SeResNet18						BLL-SeResNet18					
	Ω_m	h	σ_8	$0.1 \log_{10} f_{R0} $	$\Omega_m h^2$	$\sigma_8 \Omega_m^{0.25}$	Ω_m	h	σ_8	$0.1 \log_{10} f_{R0} $	$\Omega_m h^2$	$\sigma_8 \Omega_m^{0.25}$
MSE ↓	0.001	0.01	0.0007	0.003	0.0009	0.0008	0.003	0.013	0.0012	0.0035	0.0009	0.0013
$r^2 \uparrow$	0.86	0.15	0.94	0.04	0.85	0.93	0.80	0.03	0.90	0.008	0.85	0.89
UCE ↓	0.07	0.07	0.08	0.02	0.08	0.12	0.03	0.3	0.08	0.05	0.022	0.15
AV-MSE ↓				0.0043						0.0051		
NLL ↓				-99.21							-3.38	
Inf.Time [ms]				397							290	

Metrics	FullB-ResNet18						BLL-ResNet18					
	Ω_m	h	σ_8	$0.1 \log_{10} f_{R0} $	$\Omega_m h^2$	$\sigma_8 \Omega_m^{0.25}$	Ω_m	h	σ_8	$0.1 \log_{10} f_{R0} $	$\Omega_m h^2$	$\sigma_8 \Omega_m^{0.25}$
MSE ↓	0.001	0.01	0.0007	0.003	0.001	0.0008	0.0025	0.012	0.0015	0.003	0.0015	0.001
$r^2 \uparrow$	0.86	0.15	0.95	0.04	0.83	0.93	0.82	0.10	0.89	0.05	0.75	0.92
UCE ↓	0.07	0.09	0.09	0.01	0.08	0.20	0.014	0.078	0.09	0.07	0.024	0.14
AV-MSE ↓				0.0043						0.0048		
NLL ↓				-95.12						-3.34		
Inf.Time [ms]				345							262	

**Fig. 6.** True vs Predicted values provided by the FullB model, for Ω_m , σ_8 , and some derivative parameters. Points are the mean of the predicted distributions, and error bars stand for the heteroscedastic uncertainty associated with epistemic and aleatoric uncertainty at 1σ .**Table 4.** Configuration of the fully connected neural network used for constraining parameters from the power spectrum.

Fully connected neural network		
Layer Name	Input Shape	Output Shape
Dense Layer	(N_{batch} , 85)	(N_{batch} , 64)
ReLU	(N_{batch} , 64)	(N_{batch} , 64)
Dense Layer	(N_{batch} , 64)	(N_{batch} , 64)
ReLU+Batch Norm	(N_{batch} , 64)	(N_{batch} , 64)
Dense Layer	(N_{batch} , 64)	(N_{batch} , 64)
ReLU	(N_{batch} , 64)	(N_{batch} , 64)
Dense Layer	(N_{batch} , 64)	(N_{batch} , 14)
Multivariate normal	(N_{batch} , 14)	(N_{batch} , 4)

however, would require additional tests of the BNN with a reduced parameter space in addition to isolating the impact of the sole case of a zero f_{R0} , which we leave for future work.

5.3. Comparison among approaches based on marginalized parameter constraints

Finally, we choose one example from the test set to compare the constrain contours predicted by the best models presented in the paper so far. Fig. 7 compares the parameter constraints at 68% and 95% confidence levels predicted for the FullB-SeResNet18 and FullB-FCN models. The true values of the example are reported in Table 6 as well as represented by dashed lines in the triangular plot. Notice that both models yield decent predictions for the marginal distribution, but they differ in the correlation among cosmological parameters, as σ_8 and f_{R0} where this be-

Table 5. Metrics for the power spectra test set with Fully-Connected Networks (FCN). High UCE values indicate miscalibration. MSE and NLL are computed only over the cosmological parameters. Bold text is the minimum (maximum) value, ↓ (↑) as indicated in the metric name, among the different parameters.

Metrics	FullB-FCN						BLL-FCN					
	Ω_m	h	σ_8	$0.1 \log_{10} f_{R0} $	$\Omega_m h^2$	$\sigma_8 \Omega_m^{0.25}$	Ω_m	h	σ_8	$0.1 \log_{10} f_{R0} $	$\Omega_m h^2$	$\sigma_8 \Omega_m^{0.25}$
MSE ↓	0.0023	0.012	0.0007	0.003	0.0013	0.0011	0.0023	0.011	0.00078	0.0030	0.0012	0.0012
r^2 ↑	0.83	0.11	0.94	0.06	0.77	0.90	0.83	0.16	0.94	0.073	0.80	0.89
UCE ↓	0.026	0.12	0.022	0.022	0.026	0.092	0.023	0.15	0.017	0.023	0.016	0.10
AV-MSE ↓				0.0045						0.0043		
NLL ↓				64.86							1.80	
Inf.Time [ms]				3.01							2.21	

Table 6. Parameters in the 95% intervals taken from the parameter constraint contours from one example of MG simulations test set predicted by the FullB-SeResnet18 and FullB-FCN.

Parameter	SeResNet18	FCN	Target
Ω_m	$0.36^{+0.13}_{-0.13}$	$0.37^{+0.12}_{-0.12}$	0.3865
h	$0.69^{+0.23}_{-0.21}$	$0.72^{+0.23}_{-0.23}$	0.6274
σ_8	$0.664^{+0.081}_{-0.082}$	$0.667^{+0.060}_{-0.060}$	0.6822
$0.1 \log_{10} f_{R0} $	$0.51^{+0.11}_{-0.11}$	$0.51^{+0.13}_{-0.14}$	0.5557
$\sigma_8 \Omega_m^{0.25}$	$0.512^{+0.081}_{-0.082}$	$0.519^{+0.059}_{-0.059}$	0.5379
$\Omega_m h^2$	$0.167^{+0.085}_{-0.079}$	$0.190^{+0.096}_{-0.091}$	0.1521

Table 7. Relative error comparison among different CNN approaches for MG and Λ CDM simulations. The relative error has been defined as $\delta y \equiv \Delta y/y$, where y stands for Ω_m , σ_8 and Δy is the uncertainty.

Method	$\delta\Omega_m$	$\delta\sigma_8$	Reference
CNN	0.0048	0.0053	Pan et al. (2020)
CNN	0.0280	0.0120	Ravanbakhsh et al. (2017)
VBNNs	0.2128	0.0545	Hortúa et al. (2023)
FlipoutBNN	0.2444	0.0844	Hortúa et al. (2023)
SeResNet	0.3611	0.1220	This work
FCN	0.3243	0.0900	This work

havior is more notorious. It implies clearly that 3D-convolutions extract further information beyond the linear regime that allows to constrain more tightly the parameter estimation.

6. Summary and discussion

We consider a wide range of MG simulations, varying their cosmological parameters, encompassing cosmologies with large deviations from the standard GR to parameters closest to those that mimic the dynamics of a Universe based on GR. The overdensity field of each snapshot was computed using the CIC mass assignment and subsequently, we obtained its power spectrum. To constrain the main set of cosmological parameters, we introduced a novel architecture of a BNN and designed several experiments to test its ability to predict MG cosmologies. The experiments consist of building two Bayesian networks based on stochastic layers located at either the top or at all levels of the architecture. This approach is motivated by the question of whether BNNs provide better accuracy and robustness performance when we work with full or partial network configurations. Starting from the 3D overdensity field, we found that although the FullB predicts slightly better the cosmological parameters than the BLL, the latter is accurate enough to retrieve cosmological information from the density field, especially for Ω_m and σ_8 . Similarly, we tested BNNs using the two-point statistics described by the power spectrum for reasonable scales limited by the Nyquist fre-

quency. The results of this experiment show that the information learned by the networks can predict the parameters with similar accuracy to the 3D field. Both configurations of the BNN architectures fall short of capturing both the Hubble parameter and the MG effects. This underscores the necessity of improving the training dataset in terms of resolution and scale for the 3D density setup. Despite the slight constraints for some cosmological parameters, the methodology can be relevant in applications where it is combined with classical inference methods (Hortúa et al. 2020b). The multiplicative normalizing flows technique in BNNs employed in this paper has proved to bring well predictions and accurate uncertainty estimates thanks to the ability to transform the approximate posterior into a more expressive distribution consistent with the data complexity. This is a significant improvement compared to standard VI where the posterior is restricted only to a Gaussian configuration. Nevertheless, the effect of assuming a Gaussian prior distribution of the weights under this approach is still unknown (Fortuin et al. 2022). In future work, we will explore Multiplicative normalizing flows with different prior distributions over the weights and analyze how the prior influences the uncertainty calibration and performance.

The finding that the MG parameter is poorly predicted when using the information provided by the density field demonstrates, on the one hand, the effectiveness of the chameleon screening mechanism in mimicking the Λ CDM model, as well as the need for further analysis with other datasets more sensitive to the effects of MG. It should be noted that in our study we have considered parameters that produce the same effect, *i.e.*, that are degenerate. Therefore, it is not straightforward to attribute a single characteristic of the overdensity field exclusively to a single parameter, as in the case of f_{R0} and σ_8 . The proposed architectures are sufficiently general from a statistical standpoint to estimate posterior distributions. However, this study has revealed that the available information is inadequate to predict all parameters solely from a single source. This underscores the significance of resolving degeneracies between cosmological parameters by incorporating supplementary data or diverse features present in the cosmological simulations. Such an approach enables the BNNs to gain a richer learning phase and parse out the signals of each cosmology. This task will be the focus of a forthcoming paper, where we plan to evaluate the BNNs robustness using simulations of higher resolution and more intricate datasets in redshift space, incorporating velocity information alongside particle positions.

In Table 7, we also present a comparison of the relative errors for the two best-estimated parameters using CNN and N-body simulations from the literature. We observed significant discrepancies in the relative errors of σ_8 and Ω_m , approximately 90% when Bayesian inference is not employed (see Ravanbakhsh et al. 2017; Pan et al. 2020). This outcome arises from using solely Λ CDM simulations in both training and test datasets, in

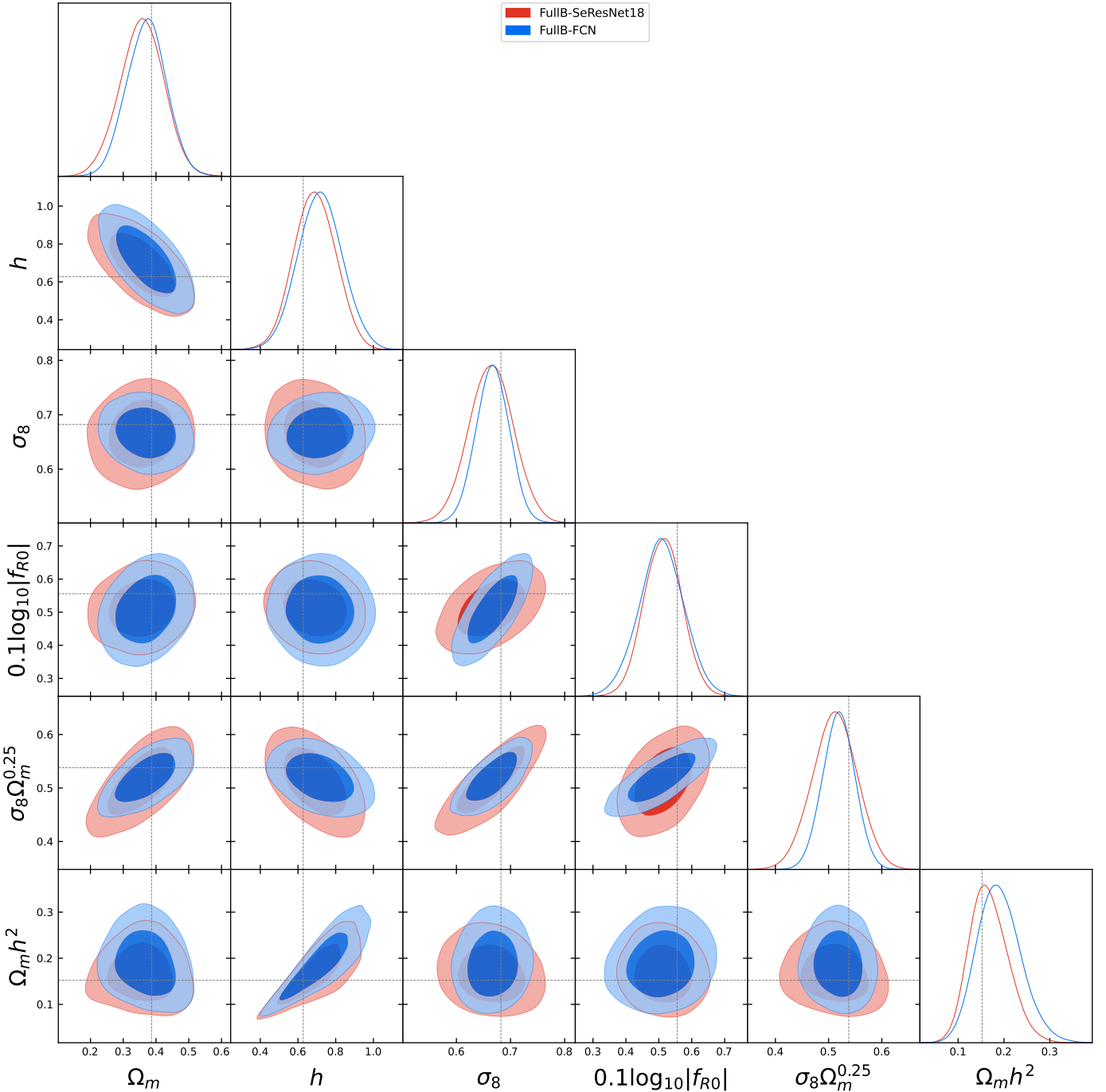


Fig. 7. 68% and 95% parameter constraint contours from one example of the test dataset using FullB-SeResNet and FullB-FCN. The diagonal plots are the marginalized parameter constraints, and dashed lines stand for the true values reported in Table 6. We derive these posterior distributions using GetDist (Lewis 2019).

contrast to our estimates that encompass an additional parameter accounting for MG and include a calibration procedure of the uncertainties. Furthermore, when contrasting the performance of BLL architectures on MG and Λ CDM simulations, such as QUIJOTE (see *e.g.* Hortúa et al. 2023), we find a deviation of the relative errors close to 30% when modified gravity effects are not considered. This result clarifies that when utilizing FullB-SeResNet18, the errorbars for Ω_m are 1.3 times larger and for σ_8 are 2.1 times larger in comparison to FlipoutBNN. In the context of BNNs, when separately considering the two cosmologi-

cal models — MG and Λ CDM — we assess the performance in terms of the MSE metric, comparing it to the results presented by Hortúa et al. (2023), who employed a similar architecture. Specifically, using FullBs in both cosmological models, we observe an improvement by a factor 13 in the MSE of the MG predictions over the Λ CDM ones. The r^2 metric was used to compare the confidence range of the individual parameters. In terms of this metric, we report that σ_8 has a larger deviation ($r^2 = 0.95$ in MG and $r^2 = 0.99$ in Λ CDM), which accounts for 4.2% of the expected uncertainty. The marginal difference in the coefficient

of determination for predicting Ω_m is only 0.01 when comparing the results of the model trained with MG against the one trained with Λ CDM. In both cases, it is noteworthy that a high r^2 value does not necessarily confer complete certainty regarding individual parameter estimates, particularly when parameter degeneracy is taken into account. Furthermore, one interesting possibility to refine the constraints on $f(R)$ gravity is given by training a specialized network that distinguishes entirely between Λ CDM and $f(R)$, offering the potential to detect a non-zero f_{R0} . Further investigations, including high-resolution simulations as well as extensions beyond Λ CDM, promise to further enhance the capabilities of the BNNs approach. The techniques explored in this work still need further developments to be applied to observational data. The bias and peculiar motions of the tracers and the systematics coming from galaxy surveys still need to be taken into account. They could be nonetheless, potentially, implemented in Bayesian inference algorithms of the large-scale structure (such as, e.g., Kitaura et al. 2021). Alongside this paper, we make available the scripts which can be accessed at the github repository <https://github.com/JavierOrjuela/Bayesian-Neural-Net-with-MNPs-for-f-R->.

7. Conclusions

One of the intriguing possibilities for explaining the observed accelerated expansion of the Universe is the modification of general relativity on large scales. Matter distribution analysis via N-body simulations offers a perfect scenario for tracking departures from standard gravity. Among different parametrizations, $f(R)$ has emerged as an interesting model due to its ability to reproduce the standard model's predictions accurately. In this manuscript, we analyzed the possibility of using Bayesian Deep Learning methods for constraining cosmological parameters from modified gravity simulations. Below, we summarize the main take-aways from this study:

1. BNNs can predict with higher accuracy cosmological parameters, especially for Ω_m and σ_8 from the overdensity field. However, based on the assumption of simulating boxes with $256 h^{-1} \text{ Mpc}$ to acquire MG effects on large scales, BNNs were unable to effectively extract MG patterns from the overdensity field to yield accurate $f(R)$ -parameter estimation. However when comparing parameter estimation with Λ CDM-only simulations, we find that there is a considerable underprediction of the uncertainties of σ_8 when possible modified gravity effects are not taken into account. In addition, special attention should be paid to parameter degeneracies that may be present not only in two-point statistics but in more features of the density field. We conclude that higher resolution and further intricate datasets in redshift space, incorporating velocity information alongside particle positions can be approaches that should be addressed to improve the network predictions.
2. It is observed that cosmological parameters can be recovered directly from the simulations using convolutional-based models with the potential of extracting patterns without specifying any N-point statistics beforehand. This is supported by the fact that networks trained with overdensity fields and power spectra predicted decent predictions but with distinctive correlations among the parameters. 3D-convolutions extracted supplementary information beyond the linear regime that allowed them to constrain tightly the parameter estimation.
3. We generalized the Multiplicative normalizing flows for BNNs to the 3D convolutional level, allowing us to work

with fully transformed stochastic neural networks. As a proof of concept, we ran several experiments in order to verify that this approach not only achieved the performance reached by the deterministic models but also yielded well-calibrated uncertainty estimates.

4. We probed the impact of the parameter estimation based on the Bayesian Last Layer (BLL) and fully Bayesian approaches. The results showed that fullBs provide slightly higher quality predictions along with accurate uncertainty estimates. Nevertheless, this improvement is not significant enough to prefer this approach with respect to the BLL, where the latter has the advantage of being relatively model-agnostic, easily scalable, and 2×inference time faster.

Acknowledgements. This paper is based on work supported by the Google Cloud Research Credits program with the award GCP19980904. HH acknowledges support from créditos educación de doctorados nacionales y en el exterior-Colciencias and the grant provided by the Google Cloud Research Credits program.

JEGF is supported by the Spanish Ministry of Universities, through a María Zambrano grant (program 2021-2023) at Universidad de La Laguna with reference UP2021-022, funded within the European Union-Next Generation EU. FSK and JEGF acknowledge the IAC facilities and the Spanish Ministry of Science and Innovation (MICINMINECO) under project PID2020-120612GB-I00. We also thank the personnel of the Servicios Informáticos Comunes (SIC) of the IAC.

References

- Abadi, M., Agarwal, A., Barham, P., et al. 2015, TensorFlow: Large-Scale Machine Learning on Heterogeneous Systems, software available from tensorflow.org
- Abdar, M., Pourpanah, F., Hussain, S., et al. 2021, Information Fusion, 76, 243
- Berti, E., Barausse, E., Cardoso, V., et al. 2015, Classical and Quantum Gravity, 32, 243001
- Bos, E. G. P., van de Weygaert, R., Dolag, K., & Pettorino, V. 2012, MNRAS, 426, 440
- Brown, Z., Mishtaku, G., & Demina, R. 2022, A&A, 667, A129
- Cai, Y.-C., Padilla, N., & Li, B. 2015, MNRAS, 451, 1036
- Charnock, T., Perreault-Levasseur, L., & Lanusse, F. 2022, Bayesian Neural Networks (WORLD SCIENTIFIC), 663–713
- Contarini, S., Marulli, F., Moscardini, L., et al. 2021, MNRAS, 504, 5021
- Crocce, M., Pueblas, S., & Scoccimarro, R. 2006, MNRAS, 373, 369
- Crocce, M., Pueblas, S., & Scoccimarro, R. 2012, 2LPTIC: 2nd-order Lagrangian Perturbation Theory Initial Conditions, Astrophysics Source Code Library, record ascl:1201.005
- De Felice, A., & Tsujikawa, S. 2010, Living Reviews in Relativity, 13, 3
- de Oliveira, R. A., Li, Y., Villaescusa-Navarro, F., Ho, S., & Spergel, D. N. 2020, Fast and Accurate Non-Linear Predictions of Universes with Deep Learning
- Dinh, L., Sohl-Dickstein, J., & Bengio, S. 2017, in International Conference on Learning Representations
- Dong, F., Park, C., Hong, S. E., et al. 2023, ApJ, 953, 98
- Dvorkin, C., Mishra-Sharma, S., Nord, B., et al. 2022, arXiv e-prints, arXiv:2203.08056
- Fang, W., Li, B., & Zhao, G.-B. 2017, Phys. Rev. Lett., 118, 181301
- Fiedler, F., & Lucia, S. 2023, Improved uncertainty quantification for neural networks with Bayesian last layer
- Fluri, J., Kacprzak, T., Sgier, R., Refregier, A., & Amara, A. 2018, J. Cosmology Astropart. Phys., 2018, 051
- Fortuin, V., Garriga-Alonso, A., Ober, S. W., et al. 2022, in International Conference on Learning Representations
- Gal, Y. 2016, PhD thesis, University of Cambridge
- García-Farieta, J. E., Hellwing, W. A., Gupta, S., & Bilicki, M. 2021, Phys. Rev. D, 103, 103524
- García-Farieta, J. E., Marulli, F., Moscardini, L., Veropalumbo, A., & Casas-Miranda, R. A. 2020, MNRAS, 494, 1658
- García-Farieta, J. E., Marulli, F., Veropalumbo, A., et al. 2019, MNRAS, 488, 1987
- Graves, A., ed. 2011, Practical Variational Inference for Neural Networks, ed. A. Graves, Vol. 24 (Curran Associates, Inc.)
- Gunapati, G., Jain, A., Sripathi, P. K., & Desai, S. 2022, Publications of the Astronomical Society of Australia, 39, e001
- Guo, C., Pleiss, G., Sun, Y., & Weinberger, K. Q. 2017, in Proceedings of the 34th International Conference on Machine Learning - Volume 70, ICML 17 (JMLR.org), 1321–1330

- Gupta, S., Hellwing, W. A., Bilicki, M., & García-Farieta, J. E. 2022, Phys. Rev. D, 105, 043538
- Hagstotz, S., Costanzi, M., Baldi, M., & Weller, J. 2019, MNRAS, 486, 3927
- Hamaus, N., Pisani, A., Sutter, P. M., et al. 2016, Phys. Rev. Lett., 117, 091302
- Harnois-Déraps, J., Martinet, N., Castro, T., et al. 2021, MNRAS, 506, 1623
- Henning, C., D'Angelo, F., & Grewé, B. F. 2021, Are Bayesian neural networks intrinsically good at out-of-distribution detection?
- Hernández-Aguayo, C., Hou, J., Li, B., Baugh, C. M., & Sánchez, A. G. 2019, MNRAS, 485, 2194
- Hernández-Aguayo, C., Ruan, C.-Z., Li, B., et al. 2022, J. Cosmology Astropart. Phys., 2022, 048
- Hikage, C., Schmalzing, J., Buchert, T., et al. 2003, PASJ, 55, 911
- Hockney, R. W. & Eastwood, J. W. 1981, Computer Simulation Using Particles (crc Press)
- Hortua, H. J. 2021, arXiv e-prints, arXiv:2112.11865
- Hortúa, H. J., García, L., & Castaneda, L. 2023, Front. Astron. Space Sci., 10
- Hortúa, H. J., Malagò, L., & Volpi, R. 2020a, Machine Learning: Science and Technology, 1, 035014
- Hortúa, H. J., Volpi, R., Marinelli, D., & Malagò, L. 2020b, Physical Review D, 102
- Howlett, C., Manera, M., & Percival, W. J. 2015, Astronomy and Computing, 12, 109
- Hu, J., Shen, L., Albanie, S., Sun, G., & Wu, E. 2019, Squeeze-and-Excitation Networks
- Hu, W. & Sawicki, I. 2007, Phys. Rev. D, 76, 064004
- Ivarsen, M. F., Bull, P., Llinares, C., & Mota, D. 2016, A&A, 595, A40
- Jennings, E., Baugh, C. M., Li, B., Zhao, G.-B., & Koyama, K. 2012, MNRAS, 425, 2128
- Johnson, A., Blake, C., Dossett, J., et al. 2016, MNRAS, 458, 2725
- Kacprzak, T., Kirk, D., Friedrich, O., et al. 2016, MNRAS, 463, 3653
- Kilbinger, M. 2015, Reports on Progress in Physics, 78, 086901
- Kingma, D. P. & Ba, J. 2014, arXiv e-prints, arXiv:1412.6980
- Kitaura, F.-S., Ata, M., Rodríguez-Torres, S. A., et al. 2021, MNRAS, 502, 3456
- Koda, J., Blake, C., Beutler, F., Kazin, E., & Marin, F. 2016, MNRAS, 459, 2118
- Kodi Ramanah, D., Charnock, T., Villaescusa-Navarro, F., & Wandelt, B. D. 2020, Monthly Notices of the Royal Astronomical Society, 495, 4227–4236
- Kratochvil, J. M., Lim, E. A., Wang, S., et al. 2012, Phys. Rev. D, 85, 103513
- Laszlo, I. & Bean, R. 2008, Phys. Rev. D, 77, 024048
- Lavaux, G. & Wandelt, B. D. 2010, MNRAS, 403, 1392
- Laves, M.-H., Ihler, S., Fast, J. F., Kahrs, L. A., & Ortmaier, T. 2020, in Medical Imaging with Deep Learning
- Lazanu, A. 2021, Journal of Cosmology and Astroparticle Physics, 2021, 039
- Lewis, A. 2019, arXiv e-prints, arXiv:1910.13970
- Li, B., Zhao, G.-B., Teyssier, R., & Koyama, K. 2012, J. Cosmology Astropart. Phys., 2012, 051
- Li, X.-D., Park, C., Sabiu, C. G., & Kim, J. 2015, MNRAS, 450, 807
- Louizos, C. & Welling, M. 2017, in Proceedings of the 34th International Conference on Machine Learning - Volume 70, ICML'17 (JMLR.org), 2218–2227
- Luo, X., Wu, Z., Li, M., et al. 2019, ApJ, 887, 125
- Lyall, S., Blake, C., Turner, R., Ruggieri, R., & Winther, H. 2023, MNRAS, 518, 5929
- Mancarella, M., Kennedy, J., Bose, B., & Lombriser, L. 2022, Phys. Rev. D, 105, 023531
- Merten, J., Giocoli, C., Baldi, M., et al. 2019, MNRAS, 487, 104
- Moresco, M., Amati, L., Amendola, L., et al. 2022, Living Reviews in Relativity, 25, 6
- Nojiri, S., Odintsov, S. D., & Oikonomou, V. K. 2017, Phys. Rep., 692, 1
- Paiillas, E., Cai, Y.-C., Padilla, N., & Sánchez, A. G. 2021, MNRAS, 505, 5731
- Pan, S., Liu, M., Forero-Romero, J., et al. 2020, Science China Physics, Mechanics, and Astronomy, 63, 110412
- Park, C. & Kim, Y.-R. 2010, ApJ, 715, L185
- Peebles, P. J. E. 2001, in Astronomical Society of the Pacific Conference Series, Vol. 252, Historical Development of Modern Cosmology, ed. V. J. Martínez, V. Trimble, & M. J. Pons-Bordería, 201
- Peel, A., Lalande, F., Starck, J.-L., et al. 2019, Phys. Rev. D, 100, 023508
- Peel, A., Lin, C.-A., Lanusse, F., et al. 2017, A&A, 599, A79
- Perico, E. L. D., Voivodic, R., Lima, M., & Mota, D. F. 2019, A&A, 632, A52
- Philcox, O. H. E., Slepian, Z., Hou, J., et al. 2022, MNRAS, 509, 2457
- Planck Collaboration, Aghanim, N., Akrami, Y., et al. 2020, A&A, 641, A6
- Puchwein, E., Baldi, M., & Springel, V. 2013, MNRAS, 436, 348
- Ravanbakhsh, S., Oliva, J., Fromenteau, S., et al. 2017, arXiv e-prints, arXiv:1711.02033
- Sønderby, C. K., Raiko, T., Maaløe, L., Sønderby, S. K., & Winther, O. 2016, in Proceedings of the 30th International Conference on Neural Information Processing Systems, NIPS'16 (Red Hook, NY, USA: Curran Associates Inc.), 3745–3753
- Song, Y.-S., Hu, W., & Sawicki, I. 2007, Phys. Rev. D, 75, 044004
- Takada, M. & Jain, B. 2003, MNRAS, 340, 580
- Tamosiunas, A., Winther, H. A., Koyama, K., et al. 2021, MNRAS, 506, 3049
- Tassev, S., Zaldarriaga, M., & Eisenstein, D. J. 2013, J. Cosmology Astropart. Phys., 2013, 036
- Touati, A., Satija, H., Romoff, J., Pineau, J., & Vincent, P. 2018, arXiv e-prints, arXiv:1806.02315
- Tsujikawa, S. 2008, Phys. Rev. D, 77, 023507
- Tsujikawa, S., Uddin, K., Mizuno, S., Tavakol, R., & Yokoyama, J. 2008, Phys. Rev. D, 77, 103009
- Van Waerbeke, L., Mellier, Y., Radovich, M., et al. 2001, A&A, 374, 757
- Veropalumbo, A., Binetti, A., Branchini, E., et al. 2022, J. Cosmology Astropart. Phys., 2022, 033
- Villaescusa-Navarro, F., Hahn, C., Massara, E., et al. 2020, ApJS, 250, 2
- Voivodic, R., Lima, M., Llinares, C., & Mota, D. F. 2017, Phys. Rev. D, 95, 024018
- Watson, J., Andreas Lin, J., Klink, P., Pajarinen, J., & Peters, J. 2021, in Proceedings of Machine Learning Research, Vol. 130, Proceedings of The 24th International Conference on Artificial Intelligence and Statistics, ed. A. Banerjee & K. Fukumizu (PMLR), 1198–1206
- Weinberg, D. H., Mortonson, M. J., Eisenstein, D. J., et al. 2013, Phys. Rep., 530, 87
- Winther, H. A., Koyama, K., Manera, M., Wright, B. S., & Zhao, G.-B. 2017, J. Cosmology Astropart. Phys., 2017, 006
- Zhang, H., Samushia, L., Brooks, D., et al. 2022, MNRAS, 515, 6133
- Zhang, Z., Gu, G., Wang, X., et al. 2019, ApJ, 878, 137